METALLURGICAL AND MATERIALS TRANSACTIONS A manuscript No.
(will be inserted by the editor)

A Deformation Mechanism Map for Incoloy 800H Optimized Using the Genetic Algorithm

AARON L. BEARDSLEY · CATHERINE M. BISHOP · MILO V. KRAL

Received: date / Accepted: date

Abstract A total of fifty-eight Incoloy 800H samples were creep tested between temperatures of 1023 - 1293 K, stresses of 14.1 - 105 MPa, and average grain sizes of 87.7 - 315 μm. Combined with data obtained by the National Institute for Materials Science (NIMS), a deformation mechanism map (DMM) for Incoloy 800H was produced. Optimization of the fit of the constitutive creep equations to the experimental data was performed using a global search iterative numerical optimization tool called a genetic algorithm (GA). It was found that the data were well represented by both high-temperature and low-temperature power-law creep mechanisms, but the extent of the influence of diffusion-based creep mechanisms, most specifically Coble creep, will require further investigation. A training and test method was performed to validate the solution and to test the extrapolability of the dataset. It was determined that the extrapolability of the data in all directions of the DMM was generally low.

AARON L. BEARDSLEY, Postdoctoral Fellow, CATHERINE M. BISHOP, Associate Professor, and MILO V. KRAL, Professor, are with the University of Canterbury Mechanical Engineering Department, Christchurch, New Zealand. Contact e-mail: albeardsley@hotmail.com

1. Introduction

1.1. Incoloy 800H

Incoloy 800H is an austenitic stainless steel alloy first developed in the 1950s with a nominal composition of Fe-32Ni-21Cr-1.5Mn-1.0Si-0.4Ti-0.4Al and a carbon content of 0.05 - 0.10%.[1,2] It has a solid solution strengthened FeNiCr matrix with additional strengthening from $M_{23}C_6$ and Ti(C,N) precipitates.[3] 800H is commonly used in high temperature applications due to its high resistance to corrosion[4,5] and creep.[6,7] In particular, it is used in the petrochemical industry for methane reformer exit tubing.[8,9] It was also short-listed as a candidate for high temperature components in next generation nuclear reactor systems.[10]

1.2. Creep and Creep Mechanisms

Creep is the inelastic deformation of a material under sustained load at elevated temperatures.[11] The temperature at which creep becomes relevant is typically above 0.4 - 0.5 T_m,[12,13] where T_m is the absolute melting point of the material. The term creep encompasses a number of different high temperature deformation mechanisms. These mechanisms are often described analytically using the minimum strain-rate (also known as the secondary creep rate), $\dot{\varepsilon}_{min}$, as a function of temperature, T, shear stress, σ_s (where σ is the uniaxial test stress, and $\sigma_s = \sigma/\sqrt{3}$), and average grain size, d.[14] The creep mechanisms include, but are not limited to, low-temperature power-law creep, where the rate-controlling mechanism is the transport of matter through dislocation cores,[15,16] high-temperature power-law creep, where the rate-controlling mechanism is the climb of dislocations,[17,18] Nabarro-Herring creep, where the rate-controlling mechanism is the diffusion of vacancies through the lattice,[19,20] and Coble creep, where the rate-controlling mechanism is the diffusion of vacancies through grain boundaries.[21]

The constitutive equations for the minimum strain-rate of low-temperature power-law creep, $\dot{\varepsilon}_{LT}$, high-temperature power-law creep, $\dot{\varepsilon}_{HT}$, Nabarro-Herring creep, $\dot{\varepsilon}_{NH}$, and Coble creep, $\dot{\varepsilon}_{Co}$ are

$$\dot{\varepsilon}_{LT} = A_{LT}\frac{a_c D_{c_0} G}{bkT}\left(\frac{\sigma_s}{G}\right)^{n+2}\exp\left(\frac{-Q_c}{RT}\right) \tag{1}$$

$$\dot{\varepsilon}_{HT} = A_{HT}\frac{D_{l_0}Gb}{kT}\left(\frac{\sigma_s}{G}\right)^n \exp\left(\frac{-Q_l}{RT}\right) \tag{2}$$

$$\dot{\varepsilon}_{NH} = A_{NH}\frac{D_{l_0}Gb}{kT}\left(\frac{b}{d}\right)^2\left(\frac{\sigma_s}{G}\right) \exp\left(\frac{-Q_l}{RT}\right) \tag{3}$$

$$\dot{\varepsilon}_{Co} = A_{Co}\frac{D_{gb_0}Gb}{kT}\left(\frac{b}{d}\right)^3\left(\frac{\sigma_s}{G}\right) \exp\left(\frac{-Q_{gb}}{RT}\right) \tag{4}$$

where A_{LT}, A_{HT}, A_{NH}, and A_{Co} are constants; a_c is the effective cross-sectional area of a dislocation core; D_{c_0}, D_{l_0}, and D_{gb_0} are the pre-exponential diffusion constants for low-temperature power-law creep, high-temperature power-law creep, and Coble creep, respectively; G is the temperature-dependent shear modulus; b is the Burgers vector; k is the Boltzmann constant; n is the power-law exponent; Q_c, Q_l, and Q_{gb} are the activation energies for low-temperature power-law creep, high-temperature power-law creep, and Coble creep, respectively; and R is the universal gas constant.

The total minimum strain-rate is evaluated by summing the contributions of each of these mechanisms together, Eq. [5]. The mechanism that provides the largest contribution to the total minimum strain-rate is considered the dominant mechanism.

$$\dot{\varepsilon}_{min} = \dot{\varepsilon}_{LT} + \dot{\varepsilon}_{HT} + \dot{\varepsilon}_{NH} + \dot{\varepsilon}_{Co} \tag{5}$$

1.3. Deformation Mechanism Maps

In 1965, Weertman and Weertman[22] first put forward the idea of graphically representing the creep deformation performance of materials by plotting isominimum strain-rate lines on a two-dimensional map with normalized shear stress (σ_s/G) on the vertical axis and homologous temperature (T/T_m) on the horizontal axis with average grain size held constant. Later further developed by Frost and Ashby,[14] this came to be known as a deformation mechanism map (DMM), on which separate regions can be indicated to illustrate which creep mechanism is the dominant mechanism for any given temperature and stress. The boundaries between regions correspond to combinations of temperature and stress where the minimum strain-rates of the two mechanisms are equal. These DMMs are used to quickly ascertain the expected minimum strain-rate and deformation mechanism of a material for a given application with known conditions, or to determine the appropriate conditions in order to achieve a desired minimum strain-rate.

Creep data for 800H have been presented using the Larson-Miller relationship,[1,23–26] which plots the Larson-Miller parameter, LMP, against applied stress, where LMP is defined as

$$LMP = T(C_{LM} + \log_{10}(t_r)) \tag{6}$$

where C_{LM} is a constant that is typically on the order of 20, independent of the material,[11], and t_r is the time to rupture in hours. Creep data for 800H has also been presented using the Monkman-Grant relationship,[27], which is defined as

$$\dot{\varepsilon}_{min}{}^{m_{MG}} t_r = K_{MG} \tag{7}$$

where m_{MG} is a constant on the order of unity, and K_{MG} is a constant on the order of 10^{-2} - 10^{-1}. Swindeman and Marriott[28] provided a graph of rupture time versus minimum strain-rate for 800H, but did not supply the resulting Monkman-Grant constants. This graph was digitized and a best-fit line was used to estimate Monkman-Grant constants of $m_{MG} = 0.69$ and $K_{MG} = 0.84$.

The Larson-Miller and Monkman-Grant relationships do not provide any information about the creep deformation mechanism involved or the effect of average grain size, which is a role that can be filled by creating a DMM. For this purpose, the constants of the constitutive creep equations have been determined or estimated for a large number of materials,[14] but, despite being used extensively for creep-limited applications, no attempt has yet been made to obtain all of the constants and subsequently create a DMM for 800H.

1.4. Optimization

In order to create a DMM for an alloy, the values of each of the material-specific constants in the constitutive equations must be estimated. This is preferably performed by fitting the constants to a statistically significant number of experimental creep data. In the past, this procedure has typically been performed analytically.[14] For example, experimental data can be separated into temperature groups and plotted on a graph of $\ln(\dot{\varepsilon}_{min})$ versus $\ln(\sigma_s/G)$. A best-fit line can then be placed through each temperature group where the gradient of the best-fit line provides an estimate for the power-law exponent. Similarly, experimental data can be separated into stress groups and plotted on a graph of $\ln(\dot{\varepsilon}_{min})$ versus $-1/(RT)$. A best-fit line can then be placed through each stress group where the gradient of the best-fit line provides an estimate for the activation energy for creep. The remaining constants can be

estimated using similar methods. A small fraction of examples of this approach from within the last decade include Ueda *et al.*,[29] Matsunaga *et al.*,[30] Kawasaki and Langdon,[31] and Chawake *et al.*[32]

The analytical approach contains a number of significant flaws. It involves several subjective assumptions, most particularly when estimating *a priori* where the changes in the dominant mechanism occur in the data before fitting. Also, by separating the experimental data into temperature or stress groups, multiple values for the power-law exponent or activation energy for creep are obtained. These need to be processed further using a weighted average if a global value is to be provided. This grouping of data also requires that small, unavoidable differences in temperature or stress between different creep tests are ignored. Ultimately, the largest issue is that the analytical method does not obtain the optimum fit of the constitutive equation constants to the experimental data.

To overcome these issues, the equations can be solved numerically using an optimization tool. One such example is the neural network technique utilized by Bano *et al.*[33] In the present work, a genetic algorithm (GA) was applied. The GA is an iterative, metaheuristic, global search computational optimization technique developed by Holland in 1975.[34] The GA follows a five stage procedure of initialization, fitness evaluation, parent selection, breeding, and termination, Figure 1, which will be briefly summarized here. A detailed description of the processes and characteristics of the GA have been given in the literature,[35] so only a brief description will be provided here as to cover some of the heuristic devices relevant to this application. Two of the primary benefits of this tool are that it can be easily expanded to incorporate alternative creep equations when necessary, and that it can be applied to a creep test dataset for any material.

1.5. Novelty

This paper uses new and published experimental creep test data to provide the first DMM for the industrially-relevant alloy 800H. We demonstrate the optimization of the constitutive creep equations to experimental data using a GA for the first time. This tool is further utilized by using a training and test method to simultaneously validate the model and assess the extrapolability of the creep test data.

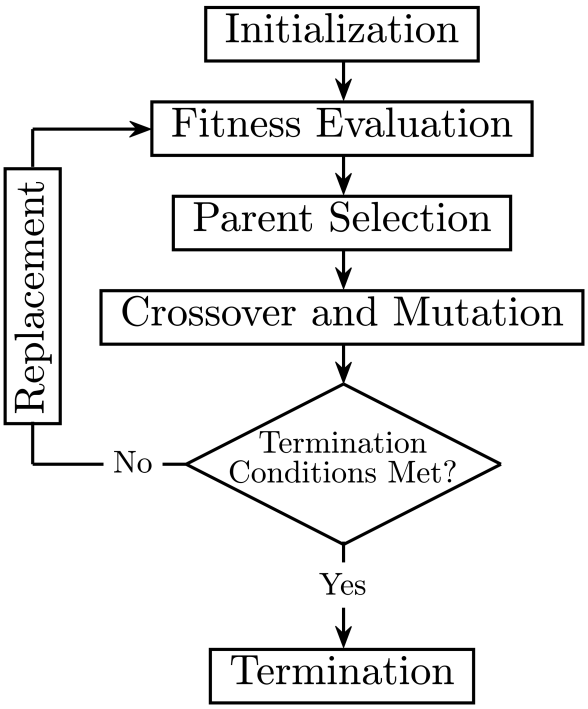

Fig. 1: Flow diagram for a simple GA.

2. Experimental

2.1. Sample Preparation and Assessment

Microscopy was performed on a Japan Electron Optics Ltd. JSM-IT300LV LaB_6 electron gun scanning electron microscope using an accelerating voltage of 20 keV. It is equipped with an Oxford Instruments (OI) X-Max™ silicon drift solid-state energy-dispersive X-ray spectroscopy (EDS) detector and an OI HKL Nordlys III electron backscatter diffraction (EBSD) detector, both of which are operated using OI AZtecHKL software.

Raw 800H material was received in an as-pilgered condition from Tubacex, Spain. The tube had an outer diameter of 42 mm and a wall thickness between 6.0 - 6.5 mm. From multiple large-area EDS measurements with a detector-optimized working distance of 15 mm and an approximate dead-time of 50%, the tube was found to have an average composition of Fe-30.5Ni-21.4Cr-1.0Mn-0.5Ti-0.3Al-0.1Si, which is within the specifications for the American Society for Testing and Materials International (ASTM) standard B 407.[2]

A 2 hour heat-treatment was performed on separate tube sections at either 1373 K, 1423 K, or 1473 K in order to solutionize the material and create samples with a range of average grain sizes. All heat-treatments were followed by an immediate quench in room-temperature water.

Creep test samples were cut from the wall of the tubes in the axial direction. The samples,

designed according to ASTM standard E8,[36] had a gauge length of 30 mm and a rectangular cross-section with a width of 4.0 mm and a thickness of 3.1 mm.

In order to estimate the average grain size of each creep test sample, additional samples were taken from the tube near to where the gauge length of each creep test sample was cut. These samples were mounted in Buehler ProbeMet™ conductive mounting compound using a Buehler SimpliMet® 3000 automatic mounting press. Polishing was performed on a Buehler Vector® LC 250 power head semi-automatic grinder-polisher using traditional methods, with a final polish of 0.06 μm using MasterMet™ colloidal silica suspension.

EBSD maps of samples heat-treated at 1373 K were obtained with a step size of 4.0 μm over an area of 1.5 mm^2. EBSD maps of samples heat-treated at 1423 K and 1473 K were obtained with a step size of 6.0 μm over an area of 4.0 mm^2. It was necessary to increase the map area for samples heat-treated at higher temperatures in order to obtain a sufficient number of grains in each map and satisfy the requirements of ASTM standard E2627.[37] The EBSD maps were then processed to replace misindexed and unindexed pixels according to ASTM standard E2627 using a custom-built MATLAB® (R2017a) code. The same code then computationally applied the ASTM standard E112 circle intercept method to obtain the average grain size.[38] As specified in the standard, Σ3 boundaries were excluded during the grain size measurement process. The average grain sizes of the creep test samples ranged from 87.7 - 315 μm. These measurements had an approximate 95% confidence interval of ± 9 μm, which was obtained by measuring three EBSD maps on the same sample in different locations.

2.2. Creep Testing

Creep tests were performed according to ASTM standard E139 in a custom-built creep test apparatus.[39] A total of fifty-eight samples were tested. Test temperatures ranged from 1023 - 1293 K, where temperature was controlled to ± 4 K using N-type thermocouples. Test stresses ranged from 14.1 - 105 MPa. Stress was controlled to approximately ± 3%, where test load was measured using OMEGA™ LC201 0.75 inch subminiature tension and compression load cells, and gauge length cross-sectional area measurements were performed using digital Vernier calipers. Creep tests were performed with times ranging from 10 - 2000 hours. Of the fifty-eight tests, twenty-four were performed until rupture, and the remainder were terminated after the onset of tertiary creep in order to conserve time.

2.3. Extraction of Minimum Strain-Rate

Sample extension during creep testing was measured using an AMETEK® OP-6.0 linear variable differential transformer. The measurement of strain versus time, such as in the first 25 hours of a creep test shown in Figure 2, contains fluctuations that were attributed to the changes in ambient temperature of the room and the temperature control of the creep testing apparatus. The initial strain from loading was ignored here as it does not affect the minimum strain-rate and simplifies the analysis. In order to extract the minimum strain-rate, the raw data were fitted to a hyperbolic-sine power-law equation[40] in the form of

$$\varepsilon(t) = H_1(\sinh(H_2 t))^{H_3} \tag{8}$$

where ε is strain, t is time, H_1, H_2 and H_3 are fitted constants with the restriction $0 \leq H_3 \leq 1$. The fitting was performed using the nonlinear least-squares curve-fitting tool '*lsqcurvefit*' in MATLAB. Curve-fitting was performed using both the trust-region-reflective and Levenberg-Marquardt methods, both of which attained the same solution in every case. This equation achieved significantly better fits than the Andrade equation and related equations.[11] However, it should be noted that this equation is only capable of modeling up to the onset of tertiary creep. The decision of how much data to fit to the equation was determined subjectively, which is one of the current limitations of this method. This is primarily due to the wide variety in the shape of creep curves and the amplitude of fluctuations, which makes it difficult to define a specific tolerance value for the fit of Eq. [8]. The minimum strain-rate is obtained analytically from Eq. [9].

$$\dot{\varepsilon}_{min} = H_1 H_2 \sqrt{H_3} \left(\frac{1 - H_3}{H_3} \right)^{\left(\frac{H_3 - 1}{2}\right)} \tag{9}$$

2.4. Data

The test conditions and extracted minimum strain-rates for all fifty-eight samples are given in Table 1. In this table, samples are labeled according to their heat-treatment temperature (*i.e.* Sample 1100 - 1 was heat-treated at 1100 °C). Ten samples, labeled 0 - 1 through 0 - 10, were made from annealed 800H plate, as received from VDM Metals, Australia. Rupture times are given for the twenty-four creep test samples that were performed until rupture. The time taken for samples to reach 2% strain, $t_{2\%}$, is also provided where available.

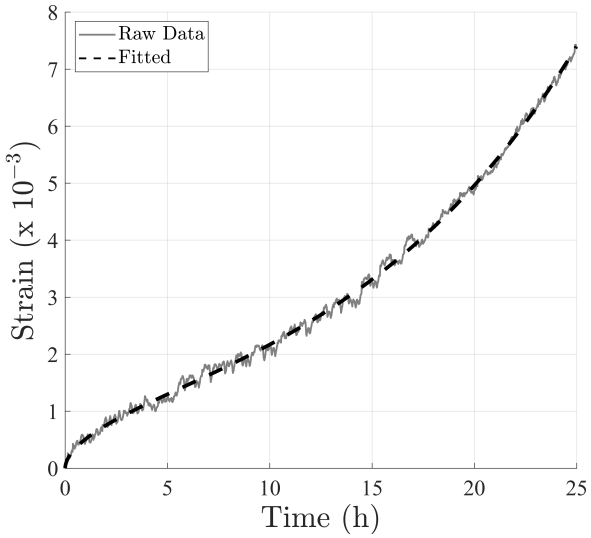

Fig. 2: Raw creep plastic strain data and fit to Eq. [8] for Sample 1100 - 12 (see Table 1 for sample information).

Table 1: Creep Sample Test Temperature, T, Uniaxial Stress, σ, Average Grain Size, d, and Determined Values of Minimum Strain-Rate, $\dot{\varepsilon}_{min}$, Rupture Time, t_r, and Time to 2% Strain, $t_{2\%}$

Sample	T (°C)	σ (MPa)	d (μm)	$\dot{\varepsilon}_{min}$ (x 10^{-9} s^{-1})	t_r (h)	$t_{2\%}$ (h)
0 - 1	1000	23.4	143	217	43.3	9.14
0 - 2	906	24.0	165	2.52	-	-
0 - 3	1000	24.0	159	169	44.3	9.41
0 - 4	1000	17.2	161	23.1	-	-
0 - 5	900	45.9	165	140	42.5	12.0
0 - 6	906	30.0	153	7.44	-	115
0 - 7	1000	17.9	142	35.4	-	-
0 - 8	900	24.4	174	2.29	-	-
0 - 9	900	38.3	239	30.5	-	41.0
0 - 10	900	47.8	208	297	23.9	7.91
1100 - 1	957	24.7	87.7	12.6	-	86.0
1100 - 2	957	24.3	115	19.8	-	106
1100 - 3	950	18.2	88.0	5.24	-	327
1100 - 4	950	18.4	87.8	8.34	809	250

1100 - 5	801	75.3	90.9	118	-	35.8
1100 - 6	750	78.1	103	4.08	794	310
1100 - 7	850	40.8	87.9	6.26	490	269
1100 - 8	1000	15.6	96.7	37.6	-	65.7
1150 - 1	750	64.0	187	0.512	-	-
1150 - 2	759	105	183	198	86.7	21.6
1150 - 3	1020	17.6	193	47.7	-	49.4
1150 - 4	850	39.9	187	3.59	680	404
1150 - 5	950	25.9	165	7.91	258	148
1150 - 6	950	25.5	162	5.92	362	194
1150 - 7	962	18.3	170	5.16	-	334
1150 - 8	962	18.2	168	6.36	-	317
1200 - 1	950	18.1	254	3.50	-	-
1200 - 2	956	24.6	237	16.5	-	137
1200 - 3	950	17.4	315	2.89	-	-
1200 - 4	956	23.0	272	14.9	-	136
1200 - 5	861	39.8	194	3.50	576	378
1200 - 6	861	45.9	217	24.0	110	79.8
1200 - 7	759	94.2	227	47.6	-	66.8
1200 - 8	1020	18.1	231	43.9	-	52.8
1100 - 9	962	26.3	144	29.7	-	47.3
1100 - 10	962	32.3	105	101	-	19.7
1100 - 11	1000	26.0	115	181	-	18.5
1100 - 12	951	33.4	115	46.0	83.3	39.0
1100 - 13	816	42.0	109	1.38	-	1220
1100 - 14	816	46.2	131	2.70	-	844
1100 - 15	801	64.0	129	67.7	-	75.1
1100 - 16	851	53.2	141	89.8	-	60.5
1150 - 9	951	25.8	172	11.6	256	145
1150 - 10	1000	26.7	172	132	47.2	19.8
1150 - 11	956	34.4	186	205	50.9	14.6
1150 - 12	956	37.6	183	318	-	7.72

1150 - 13	1000	14.1	205	12.9	511	142
1150 - 14	815	63.2	190	220	150	20.6
1150 - 15	815	61.7	175	119	196	45.4
1150 - 16	851	52.5	182	65.4	-	75.9
1200 - 9	951	27.0	271	20.1	325	206
1200 - 10	1010	31.8	232	1610	-	2.77
1200 - 11	1010	26.7	302	137	-	13.3
1200 - 12	951	29.1	254	31.8	138	72.1
1200 - 13	801	39.0	236	0.204	-	-
1200 - 14	801	62.8	235	20.6	-	181
1200 - 15	858	54.1	261	142	120	35.8
1200 - 16	858	61.4	225	346	59.3	13.3

The data in Table 1 were added to 159 data provided by the National Institute for Materials Science (NIMS) for subsequent analysis.[41] This makes a total of 217 data. The creep test data from NIMS were obtained at temperatures of 873 - 1323 K, and stresses of 5 - 294 MPa. The specified average grain sizes varied from 93.0 - 162 μm. Only the rupture time, rather than the minimum strain-rate, was provided for all of the 159 data. Hence, the minimum strain-rate was approximated for all data using the Monkman-Grant equation and the constants specified in Section 1.3. These constants were deemed appropriate as they were generated using NIMS 800H data. However, the source did not specify whether they used 800H tube, plate, rod, or some combination of the three types.[28] This provides a source of uncertainty in the results.

3. Analysis with Genetic Algorithm

3.1. Input Equation

The selected creep mechanisms for this analysis were low-temperature power-law, high-temperature power-law, Coble and Nabarro-Herring, as these have been well documented to be relevant for similar alloys near the temperatures and stresses that were tested in the present work.[14] The efficiency of the GA is maximized by minimizing the

number of required operations. Therefore, the input equation (Eq. [5]) was simplified as much as possible by combining like terms, resulting in

$$\dot{\varepsilon}_{min} = A_1 K_1 \exp\left(\frac{A_6}{K_6}\right) + A_4 K_4 K_5{}^{(A_5+2)} \exp\left(\frac{A_8}{K_6}\right) + (A_2 K_2 + A_3 K_3 K_5{}^{A_5}) \exp\left(\frac{A_7}{K_6}\right) \quad (10)$$

where A_{1-8} are material-specific constants which need to be optimized, with equivalents from Eqs. [1 - 4] of

$$A_1 = A_{Co} D_{gb_0} \quad (11a)$$

$$A_2 = A_{NH} D_{l_0} \quad (11b)$$

$$A_3 = A_{HT} D_{l_0} \quad (11c)$$

$$A_4 = A_{LT} a_c D_{c_0} \quad (11d)$$

$$A_5 = n \quad (11e)$$

$$A_6 = Q_{gb} \quad (11f)$$

$$A_7 = Q_l \quad (11g)$$

$$A_8 = Q_c \quad (11h)$$

and K_{1-6} are known values which correspond to the following equations

$$K_1 = \frac{\sigma_s b^4}{kTd^3} \quad (12a)$$

$$K_2 = \frac{\sigma_s b^3}{kTd^2} \quad (12b)$$

$$K_3 = \frac{Gb}{kT} \quad (12c)$$

$$K_4 = \frac{G}{bkT} \quad (12d)$$

$$K_5 = \frac{\sigma_s}{G} \quad (12e)$$

$$K_6 = -RT \quad (12f)$$

The Burgers vector was estimated to be $b = 2.53 \times 10^{-10}$ m based on a weighted average of the values for iron, nickel and chromium.[14] The temperature-dependent shear modulus was approximated by placing a best-fit second-order polynomial through tensile test data provided by Special Metals,[1] which was determined to be

$$G = -5.38 \times 10^3 T^2 - 2.13 \times 10^7 T + 8.00 \times 10^{10} \quad (13)$$

This model encompasses the region of the DMM below the plasticity line, the line above which the dominant mechanism changes to plasticity. No experimental data were collected

above the plasticity line and this region should be considered as a first approximation only. Data above the plasticity line were approximated using the constitutive equation constant values for 316 stainless steel, the most similar alloy to 800H for which data are readily available.[14] The positions of the plasticity line and the ideal shear strength line were selected to be $\sigma_s/G = 4.5 \times 10^{-3}$ and $\sigma_s/G = 6.0 \times 10^{-2}$, respectively, also based on values for 316 stainless steel. These regions of the DMM were not considered critical in this analysis and was only included for completeness.

3.2. The Genetic Algorithm Process

3.2.1. Initialization

Optimization of the constitutive creep equations was performed using a custom-built MATLAB program. To initialize the GA, each of the eight unknown constants, A_{1-8}, were encoded into a string of binary digits. The analogy for the string of binary digits for each constant is a chromosome, where the length of the string affects the number of significant figures of the solution that can be obtained and, inversely, the speed of computation. For this application, a string length of twenty digits provided a sufficiently accurate solution without significantly compromising the computation speed. The total string, a simple concatenation of each of the chromosomes, is the DNA for that member of the population. Each chromosome can be set to a specific initial value where an approximate value is known. Alternatively, each chromosome can be randomly generated in order to avoid any bias, which was the selected method in the present work. This was repeated for an n_{pop} number of members, who became the first generation population. A larger n_{pop} increases the computation time, but provides more diversity in the genetics, which reduces the probability of the solution getting trapped in a local minimum. A value of n_{pop} = 330 performed with relatively strong stability for this analysis.

3.2.2. Fitness Evaluation

The fitness evaluation is usually the most computationally demanding stage in the GA process.[34] To begin, the constants A_{1-8} were decoded from the DNA of the first member of the population. Then, using the stress, temperature, and average grain size for each experimental datum, i, Eq. [10] was evaluated. Note that the output of the equation using

the GA-calculated value was redefined here to the symbol $\dot{\varepsilon}_{calc}$, to distinguish it from the experimentally measured minimum strain-rate, $\dot{\varepsilon}_{meas}$. The fitness, δ, for this member was then calculated as the root-mean-square error between the base-10 logarithms of the two sets of values, as in

$$\delta = \sqrt{\frac{1}{N}\left(\sum_{i=1}^{N}(\log_{10}(\dot{\varepsilon}_{calc})_i - \log_{10}(\dot{\varepsilon}_{meas})_i)^2\right)} \tag{14}$$

where N is the number of experimental data. The logarithms of the minimum strain-rates were used as the error of $\dot{\varepsilon}_{min}$ exhibits a log-normal distribution, which will be demonstrated in Section 3.4. This process was repeated for each member of the population.

3.2.3. *Parent Selection*

Each member of the population was assigned a rank, R_f, according to their fitness, where the member with the smallest δ was the fittest individual and had a rank of $R_f = 1$. From the population, n_{pop} pairs of parents were then randomly selected, where the fittest members had the highest probability of selection, P_s, calculated according to

$$P_s = \frac{{n_{pop}}^{\tau}((R_f+1)^{\tau} - {R_f}^{\tau})}{({n_{pop}}^{\tau}-1){R_f}^{\tau}(R_f+1)^{\tau}}100\% \tag{15}$$

where τ is the probability exponent, and $P_s = 0$ for $R_f = n_{pop}$. This equation is a slight modification of the roulette wheel selection technique, which is the simplest of the parent selection methods.[42] The probability exponent controls the bias towards the fitter individuals for selection, where a large τ leads to fitter individuals being selected more often. This would result in a faster convergence, but a larger likelihood of the solution getting trapped in local minimum. A moderately high value of $\tau = 0.8$ performed with relatively strong stability for this analysis.

3.2.4. *Crossover, Mutation and Replacement*

Crossover is the process of creating children by breeding two parents' DNA. Each child's DNA was created by selecting each chromosome from one of its two parents. This can be performed with bias towards the fittest parent, but in this analysis, chromosomes were selected from either parent with equal probability. Following crossover, a number of randomly selected digits of each member's DNA were mutated, where mutation means that the selected digit switched from a one to a zero, or vice versa. In this analysis, a total of three digits per

chromosome were selected for mutation. As with the probability exponent, τ, the number of mutations affects the convergence speed and the probability of the solution getting trapped in a local minimum. Finally, the children replaced the parents to become the second generation.

3.2.5. Termination

The process from fitness evaluation through to crossover, mutation and replacement was repeated until the termination condition of 100,000 generations had been reached. After termination, the final solution was decoded from the fittest member throughout all generations. This means that the solution may not have been taken from the final generation.

3.3. Training and Test Datasets

A significant problem that can occur during optimization is overfitting.[43] Generally speaking, overfitting is a phenomenon that can occur in optimization where an overly complex model is used to determine a relationship in the data which would otherwise be explained by random noise, such as that from experimental errors. This is typically a symptom of a model with too many variables being used to describe too few data. The primary consequence of overfitting is that the data cannot be reliably extrapolated.

A training and test method was applied to assess whether or not overfitting occurred during the optimization process. This method involved performing trials where the total dataset was split into two: a training set and a test set. For each trial, i, the model was optimized for 50,000 generations using only the training set. Following this, the fitness for the training set, $\delta_{train,i}$, and test set, $\delta_{test,i}$, were evaluated. For each pair of training and test sets, a total of one hundred trials were performed, after which the average fitnesses, $\bar{\delta}_{train}$ and $\bar{\delta}_{test}$, were evaluated.

Measuring extrapolability required an appropriate selection of test sets. For this section of the work, only the NIMS data was used, as using the combined data would provide an uneven distribution of data as a function of position on the DMM. Five test sets were selected for analysis. The first test set used a randomly selected subset of the data, which was altered for each trial. The number of data to include in the test set was also randomized to be any number of data up to half of the full dataset. The purpose of this test set was to act as a control group. The remaining four test sets, labeled A - D, are shown in Figure 3. Test Sets A - C were designed to measure the extrapolability of the data in their respective directions, where,

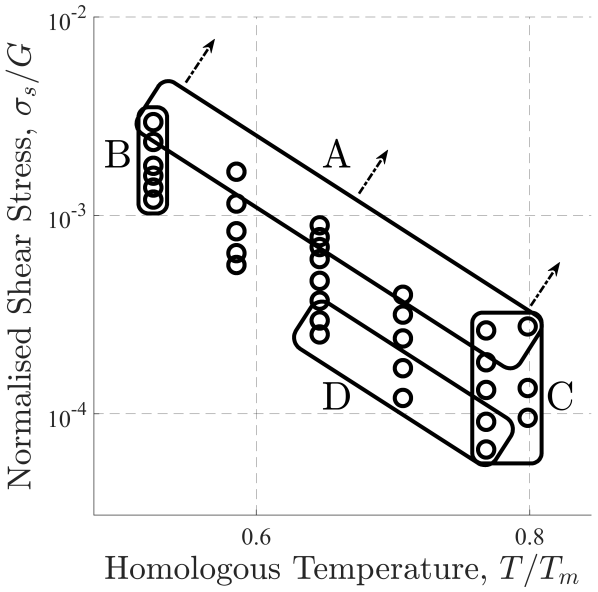

Fig. 3: Selected test sets to measure overfitting and extrapolability of the data in various directions where circles indicate the locations of experimental data. Rough extrapolability direction exemplified for Test Set A with dashed arrows.

for example, the rough extrapolability direction that Test Set A measures is indicated with dashed arrows. Test Set D contains a set of data which displayed the largest probability of being in the Coble creep mechanism region based on initial trials. This was used to test whether or not the position of the mechanism boundary between Coble creep and the other creep mechanisms shifted in the absence of these data. If the boundary shifted towards the next-nearest data, then it was evidence that the boundary may not be accurately portrayed by the GA fit of the total dataset and was only present due to overfitting.

3.4. Proof of Minimum Strain-Rate Error Log-Normal Distribution

The minimum strain-rate error is a complex function, as it is both a function of exponential inverse temperature and power-law stress. However, this section will demonstrate that this error can be approximated by a log-normal distribution. This provides justification for the log-transformation of minimum strain-rate for the GA fitness calculation, which is one of the preferred transformation methods for positively skewed data.[44] This could be conveniently demonstrated if a large number of data were collected at the same temperature and stress, which was not the case. To get around this, each set of data collected at the same temperature and stress were normalized by subtracting the mean minimum strain-rate, $\bar{\varepsilon}_{min}$, of the set

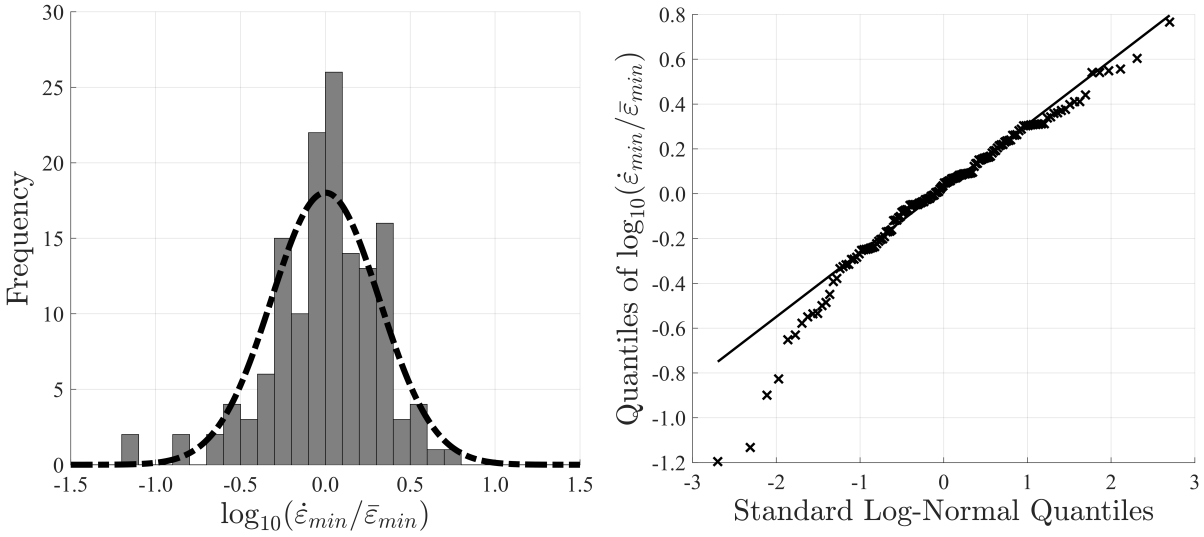

(a) (b)

Fig. 4: (a) Mean-shifted base-10 logarithm minimum strain-rate distribution with fitted log-normal distribution shown with a dashed line, and (b) corresponding QQ plot, where sample data are shown with crosses and the theoretical log-normal distribution is shown with a line.

from each datum in the set. This method necessarily assumes that the standard deviation is not a function of the mean minimum strain-rate for each data set. The resulting distribution is shown in Figure 4a, with the fitted log-normal distribution shown with a dashed line.

Visualization of the comparison between the data distribution and a standard log-normal distribution can be enhanced using a quantile-quantile (QQ) plot, which compares the quantiles of the data with the standard log-normal quantiles, Figure 4b. The QQ plot shows a good fit between the sample data and the theoretical log-normal distribution in the central region of the distribution. Deviation near the upper and lower tails are an expected anomaly in QQ plots due to outliers and the lack of sufficient data in the region. Despite this, the upper tail shows a reasonable fit. However, the lower tail indicates that the distribution of the sample data is slightly skewed from the theoretical log-normal distribution. This is not a significant problem, however, as the lower tail data are from minimum strain-rates which are smaller than the average value, meaning that the assumption that the minimum strain-rate error distribution is log-normal is an overall conservative assumption.

4. Results

4.1. Deformation Mechanism Map

Figure 5a shows the final solution DMM for 800H with an average grain size of 100 μm, a typical average grain size for this material. Figures 5b and 5c show the DMM for 800H with an average grain size of 50 μm and 350 μm, respectively, which represent the extremes of average grain sizes of tested samples.

Three creep mechanisms were found to be present based on the fit of the GA to the experimental data. These were low-temperature power-law, high-temperature power-law, and Coble creep. The inclusion of Nabarro-Herring creep in the algorithm appeared to reduce the accuracy of the solution, which was accommodated for by the GA by reducing the constant A_2 (the pre-exponential constant for Nabarro-Herring creep) to a negligible value. This indicates that the Nabarro-Herring model does not represent the behavior of 800H in the temperature and stress ranges of the collected experimental data. The absence of the Nabarro-Herring mechanism in the data is not entirely surprising as, for similar steel alloys, this mechanism is typically observed at higher T and lower σ than those used here.[14] The lack of confidence in the prediction of the constant A_2 meant that the constant was assigned a value of zero for the production of the DMMs in Figure 5. It should be noted that this does not mean that Nabarro-Herring creep does not occur for 800H. If it does become the dominant mechanism under certain conditions, those lie outside the region where experimental data were collected.

The constants from which the maps are derived are given in Table 2. These maps were generated by using the GA on the entire dataset. The fitness of the solution, evaluated by Eq. [14], was found to be 0.498. This indicates that the minimum strain-rate predicted by the solution had an error of approximately one-half of an order of magnitude from the average experimental datum. The ability of the GA to obtain a solution which accurately represents the behavior of 800H could be improved by including additional data sets from other sources.

The combination of low-temperature and high-temperature power-law mechanisms improves the solution greatly compared to when the GA is run with either mechanism individually. This is strong evidence that the two power-law mechanisms represent the behavior of the material well. Contrarily, the Coble creep mechanism contribution is small, and the solution does not change significantly when Coble creep is excluded. This implies that there is an insufficient

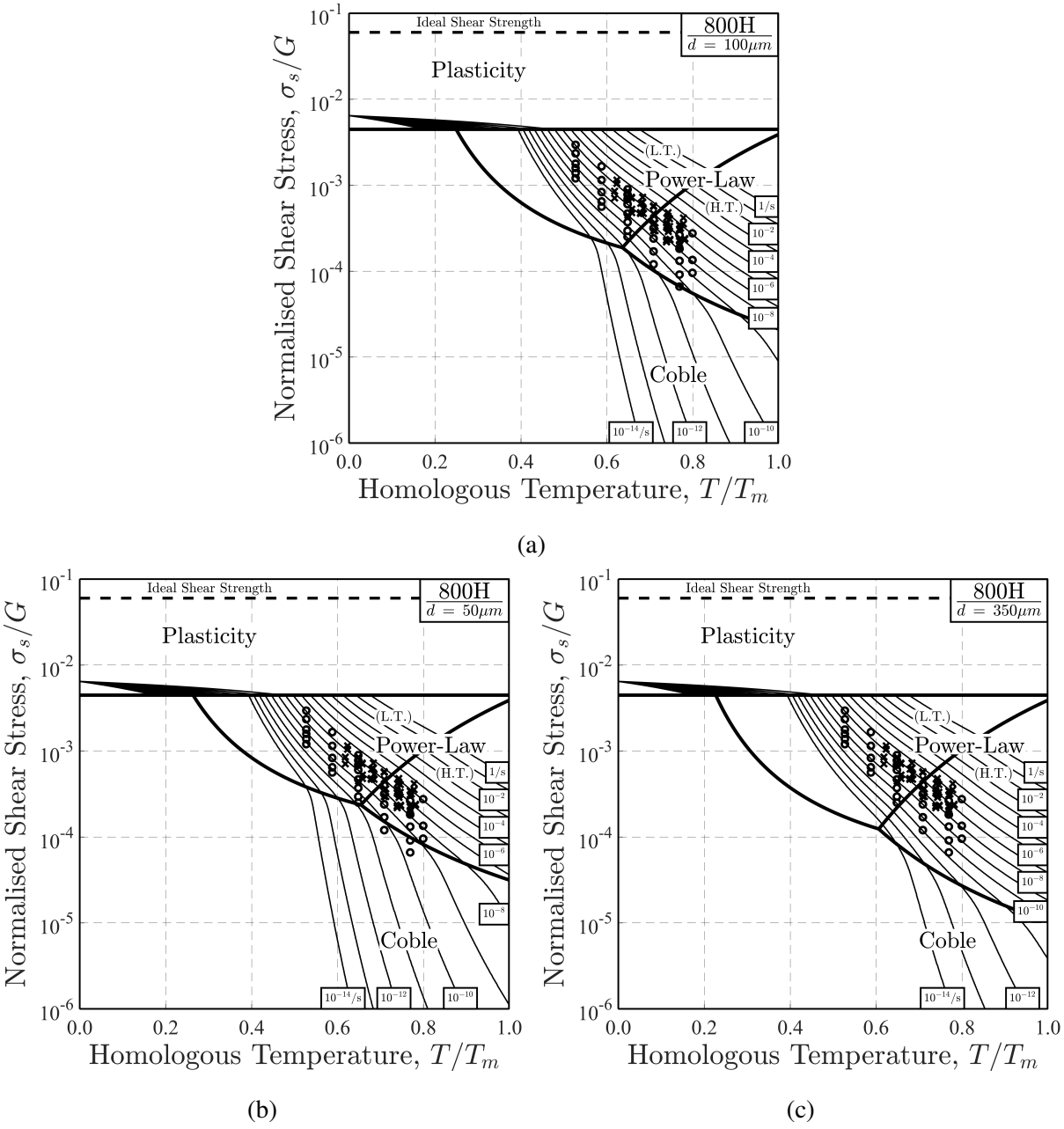

Fig. 5: DMM for Incoloy 800H with an average grain size of (a) 100 μm, (b) 50 μm and (c) 350 μm. Circles are the NIMS experimental data and crosses are the present work data. Isominimum strain-rate lines are labeled with the predicted $\dot{\varepsilon}_{calc}$.

number of experimental data in the Coble creep region of the DMM. This also means that the influence of Coble creep being detected by the GA as a result of overfitting can not be ruled out at this stage. These ideas will be explored further in Section 4.2. Creep test data in the Coble creep region of the DMM could be obtained by performing creep tests for a longer time, or at higher temperatures. However, both of these options have significant practical

Table 2: Final GA-Determined Values for Unknown Constants in Eq. [10] for Incoloy 800H, Presented to Two Significant Figures

Constant	Symbol	Value	Units
Pre-exponential for Coble creep	A_1	46	m^2s^{-1}
Pre-exponential for Nabarro-Herring creep	A_2	0	m^2s^{-1}
Pre-exponential for high-temperature power-law creep	A_3	1.6×10^{18}	m^2s^{-1}
Pre-exponential for low-temperature power-law creep	A_4	0.16	m^4s^{-1}
Power-law exponent	A_5	6.3	-
Activation energy for Coble creep	A_6	3.0×10^5	J mol^{-1}
Activation energy for high-temperature power-law creep	A_7	5.7×10^5	J mol^{-1}
Activation energy for low-temperature power-law creep	A_8	4.3×10^5	J mol^{-1}

limitations. A third, more practical, option would be to perform creep tests using samples with a smaller average grain size.

No distinct relationship between average grain size and minimum strain-rate was observed in the experimental data. This may be explained by the fact that the majority of the data lie in the power-law regime, which is independent of average grain size. However, the lack of a relationship between average grain size and minimum strain-rate was true even for the data in or near the Coble creep region of the DMM. This is further evidence against the presence of the Coble creep mechanism.

The power-law exponent was evaluated to be $n = 6.3$. Experimental observations of power-law exponents in pure metals and Class M alloys generally determine exponents of $n \approx 4.5$ - 5.0.[11,45] However, exponents up to $n = 10$ or more have been observed in complex alloys.[14] Such cases include $n = 7.9$ for 316 stainless steel,[14], $n = 7.6$ for a (Ni, Fe)Al-strengthened ferritic superalloy,[46], and $n = 9$ - 11 for Grade 91 steel.[47] Note that the latter two studies incorporated an additional constant in the form of a threshold stress (*i.e.* the term $(\sigma_s/G)^n$ was altered to $((\sigma_s - \sigma_{th})/G)^n$, where σ_{th} is a threshold stress). This can be used to manually alter the apparent stress exponent to a value that matches the expected value of $n \approx 4.5$ - 5.0. However, this method only moves the anomalous nature of the result from the constant n to the new constant σ_{th}, and may lack an appropriate justification.[48] The determined activation energy for high-temperature power-law creep of $Q_l = 5.7 \times 10^5$ J mol^{-1} also exceeds the value predicted by the physical description

Table 3: Training and Test Set Mean Fitness for One Hundred Trials

Test Set	$\bar{\delta}_{train}$	$\bar{\delta}_{test}$	$\bar{\delta}_{test} - \bar{\delta}_{train}$
Random (control)	0.365	0.411	0.046
A	0.383	0.529	0.146
B	0.357	0.524	0.167
C	0.324	0.557	0.233
D	0.354	0.601	0.247

of the model. The physical description of high-temperature power-law creep is that the rate-controlling mechanism is the climb of dislocations. Therefore, the activation energy for high-temperature power-law creep should be equivalent to the activation energy for the diffusion of vacancies through the lattice. This would predict that Q_l should be $\approx 2.5 \times 10^5$ J mol^{-1}, based on values obtained for similar alloys.[14] This increase in the apparent activation energy is also a commonly observed phenomenon in complex alloys,[49,50] including 800H.[7] These increases in the observed power-law exponent and activation energy for high-temperature power-law creep have been attributed to the influence of precipitates,[14] although a theoretical model that provides a full physical description of this phenomenon has yet to be obtained.

4.2. Validation

The mean fitnesses for each training and test set pair are given in Table 3. Identifying evidence for overfitting can be difficult and is a largely subjective process.[43] Generally, if the fitness of the test set is higher than the fitness of the training set, then it is evidence that the model is overfitting. However, since the test set was excluded from the optimization process, it is expected to produce a slightly worse fit, even in absence of overfitting. The difference in fitness between the training and test sets was smallest for the control group where randomly selected subsets of the data were excluded from the training set. This result is a strong indicator of the validity of the model and the methodology. This will be taken as a base value where values significantly larger than this will be considered to be a result of overfitting.

The difference in fitness between the training and test sets increased by at least a factor of three for Test Sets A - C compared to the control test. This indicates that the GA is indeed overfitting the data and that the extrapolability of the data is poor in all directions. Therefore, it is not advisable to use the predictions of the DMM in regions outside the area in which data are available without considering large factors of safety from the predicted value. This is particularly advisable for predictions near or over mechanism boundaries.

Test Set D was designed to determine whether or not overfitting had occurred. Specifically, this is in relation to the prediction of Coble creep becoming the dominant mechanism for a small minority of the data. When the data which were most likely to be in the Coble creep region of the DMM were excluded, the GA-determined position of the mechanism boundary between Coble creep and both power-law creep mechanisms became generally unstable. For approximately 30% of trials, the GA reduced the value of A_1 (the pre-exponential for Coble creep) to a negligible value, as it did with A_2 (the pre-exponential for Nabarro-Herring creep), which would indicate that overfitting did not occur in the original solution. However, for the remaining majority of trials, the Coble creep region shifted towards the next-nearest data, exhibiting typical overfitting behavior. This uncertainty is reflected in the difference in training and test set fitnesses for Test Set D, which was the largest among all of the assessed test sets.

The issue of overfitting for the Coble creep model would be mitigated with the addition of creep test data that were obtained further into the Coble creep region of the DMM. However, other mechanisms, such as Nabarro-Herring creep, may be present throughout the map in other regions of the DMM that do not yet contain creep test data. It is due to this nature of creep that extrapolability can never be guaranteed. This is independent of the method used to obtain the creep equation constants.

4.3. Monkman-Grant Relationship

Of the fifty-eight creep tests performed in the present work, twenty-four were performed until rupture. These twenty-four data were plotted with t_r against $\dot{\varepsilon}_{min}$, commonly known as a Monkman-Grant plot, Figure 6a. A power-law best-fit line through the data provided a coefficient of determination of 0.79. The Monkman-Grant constants from Eq. [7] were determined to be $K_{MG} = 0.82$ and $m_{MG} = 0.59$. The present work data were compared to Swindeman and Marriott data.[28]

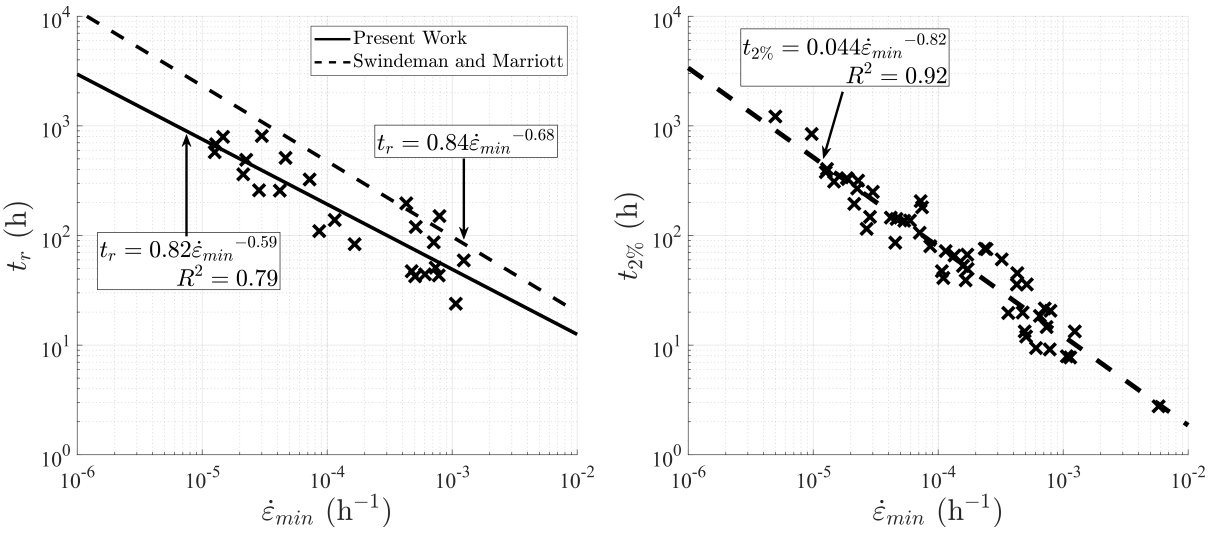

(a) (b)

Fig. 6: (a) Monkman-Grant relationship for creep test data. A best-fit line is shown for data from present work, solid, and compared to Swindeman and Marriott,[28] dashed. (b) Creep test data relationship between time to 2% strain versus minimum strain-rate, with dashed best-fit line.

Based on the best-fit lines, the present work experimental data show a rupture time decrease of approximately one-third to one-half an order of magnitude for the same minimum strain-rate compared to Swindeman and Marriott. One possible reason for this is that Swindeman and Marriott may have used 800H rod or plate instead of, or as well as, 800H tube. In the same paper, they demonstrated that 800H rod samples had superior creep performance to 800H tube, which will be verified using the Larson-Miller relationship on the NIMS data in Section 4.4. Therefore, it is likely that the ratio between minimum strain-rate and rupture time could be different for different forms of 800H. This could be due to the differences in microstructure as a result of the different forming processes. It could also be a result of compositional differences between batches.

From Figure 6a, it can be seen that the ability of the Monkman-Grant equation to predict rupture time is approximately limited to plus or minus half an order of magnitude. This is most likely a result of the large number of variables associated with tertiary creep. As demonstrated by Swindeman and Marriott, it may be preferable to use the time taken to reach 2% strain, $t_{2\%}$, instead of rupture time, Figure 6b. The correlation between the time to 2% strain and minimum strain-rate produces a much higher level of predictability, with a coefficient of determination of 0.92.

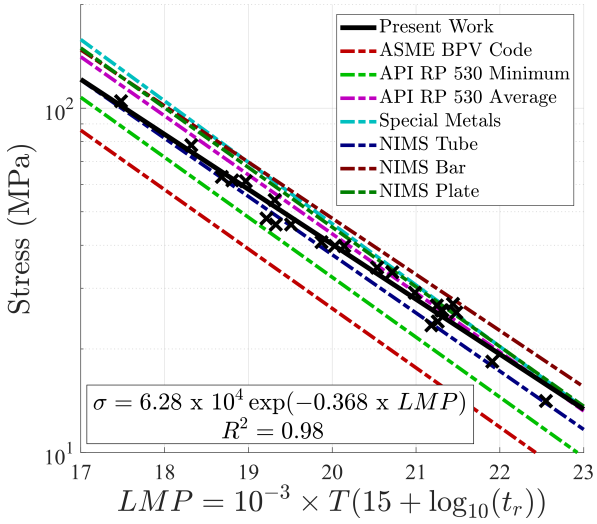

Fig. 7: Larson-Miller plot of present work data compared with data from the ASME BPV code,[25] the API RP 530 standard,[26] Special Metals,[1] and NIMS.[41,51,52] With the exceptions of the ASME BPV code data and the API RP 530 Minimum data, all lines represent average creep performance. Equation of solid best-fit line for present work data shown in lower-left corner.

4.4. Larson-Miller Relationship

Historical Larson-Miller data for 800H are available from multiple sources. The American Petroleum Institute (API) RP 530 standard[26] produced both average and minimum Larson-Miller lines for a large dataset. The API RP 530 standard used a Larson-Miller constant of C_{LM} = 15. This constant was used for all sources in order to compare the data. Other sources include the American Society of Mechanical Engineers (ASME) boiler and pressure vessel (BPV) code,[25] Special Metals,[1] and the NIMS data for 800H tube, bar and plate separately.[41,51,52] The ASME BPV code data represents an industry maximum allowable stress for creep applications. The other sources represent average creep performance values. A comparison of experimental data from the present work to the historical sets is shown in Figure 7.

An exponential best-fit line drawn through the data gave a coefficient of determination of 0.98. The data align well with NIMS tube and API RP 530 average data. Both NIMS bar and NIMS plate data exhibited longer rupture times than the NIMS tube data for the same test conditions. All of the present work data had longer rupture times than the API RP 530

minimum, indicating that the ASME BPV code guidelines are conservative for creep tests up to 2000 hours.

5. Conclusions

Numerical optimization tools, such as the GA, can be utilized for the application of DMM solving. They provide less subjective solutions compared to the traditional analytical approach. The GA also has the ability to impartially determine which creep mechanisms provide the best fit for a set of experimental creep test data, or to exclude a mechanism that does not provide an adequate fit.

A DMM has been created for Incoloy 800H using a total of 217 experimental creep test data. This is the first DMM published for the industrially-relevant alloy 800H. It was determined that the high-temperature and low-temperature power-law creep mechanisms provided an adequate fit for the majority of the obtained creep data.

For experimental data collected at relatively low stresses, the GA detected the influence of Coble creep. However, information gathered by the training and test method indicated that more data will need to be collected in the Coble creep region of the DMM in order to validate the influence of this creep mechanism. The Nabarro-Herring creep mechanism was not found to be present in any of the 800H experimental creep test data that were obtained.

This training and test method was also used to test the extrapolability of the creep test data in various directions of the DMM. It was found that the extrapolability of the data was generally low in all directions. Therefore, users of the DMM should exercise caution when estimating the minimum strain-rate of 800H outside the boundary of where creep data have been collected.

Data from the present work were compared to published data using both the Monkman-Grant relationship and the Larson-Miller relationship. For the Monkman-Grant relationship, an approximately one-third to one-half order of magnitude decrease in the expected rupture time for the same minimum strain-rate was found compared to Swindeman and Marriott data. However, for the Larson-Miller relationship, the present work data aligned well with published data.

Acknowledgements The authors wish to thank the Methanex Corporation for their continuing sponsorship of this research, and the Tubacex and Schmidt + Clemens groups for generously providing the materials for testing.

References

1. Incoloy Alloys 800H & 800HT, SMC-047, Special Metals Corporation, New Hartford, NY, 2004.

2. ASTM B 407 - 08a: *Standard Specification for Nickel-Iron-Chromium Alloy Seamless Pipe and Tube*, American Society for Testing and Materials, West Conshohocken, PA, 2008.

3. Y. Cao, H. Di, and R.D.K. Misra: *J. Nucl. Mater.*, 2014, vol. 452, pp. 77–86.

4. L. Tan, T.R. Allen, and Y. Yang: *Corros. Sci.*, 2011, vol. 53, pp. 703–11.

5. K.I. Choudhry, D.A. Guzonas, D.T. Kallikragas, and I.M. Svishchev: *Corros. Sci.*, 2016, vol. 111, pp. 574–82.

6. J.K. Wright, L.J. Carroll, C. Cabet, T.M. Lillo, J.K. Benz, J.A. Simpson, W.R. Lloyd, J.A. Chapman, and R.N. Wright: *Nucl. Eng. Des.*, 2012, vol. 251, pp. 252–60.

7. K. Natesan and P.S. Shankar: *J. Nucl. Mater.*, 2009, vol. 394, pp. 46–51.

8. H. Almostaneer, H. Schrijen, K. Barai, and A. Al-Meshari: *Advances in Materials and Processing Technologies*, 2015, vol. 1, pp. 56–66.

9. L.A. Spyrou, P.I. Sarafoglou, N. Aravas, and G.N. Haidemenopoulos: *Eng. Fail. Anal.*, 2014, vol. 45, pp. 456–69.

10. D.S. Grierson, G. Cao, P. Brooks, P. Pezzi, A. Glaudell, D. Kuettel, G. Fischer, T. Allen, K. Sridharan, and W.C. Crone: *Metall. Mater. Trans. E*, 2017, vol. 4, pp. 13–21.

11. M.E. Kassner: *Fundamentals of Creep in Metals and Alloys*, 2nd ed., Elsevier, Amsterdam, 2008.

12. F. Cao: *Mater. Sci. Eng. A*, 2015, vol. 643, pp. 169–74.

532 13. J. Vanaja, K. Laha, and M.D. Mathew: *Metall. Mater. Trans. A*, 2014, vol. 45, pp. 5076–
533 84.

534 14. H.J. Frost and M.F. Ashby: *Deformation Mechanism Maps: The Plasticity and Creep of*
535 *Metals and Ceramics*, Pergamon Press, Oxford, UK, 1982.

536 15. E.W. Hart: *Acta Metall.*, 1957, vol. 5, p. 597.

537 16. S.L. Robinson and O.D. Sherby: *Acta Metall.*, 1969, vol. 17, pp. 109–25.

538 17. J. Weertman: *J. Mech. Phys. Solids*, 1956, vol. 4, pp. 230–34.

539 18. J. Weertman: *Trans. Metal. Soc. AIME*, 1963, vol. 227, pp. 1475–76.

540 19. F.R.N. Nabarro: *Report of a Conference on the Strength of Solids*, The Physical Society,
541 London, 1948.

542 20. C. Herring: *J. Appl. Phys.*, 1950, vol. 21, pp. 437–45.

543 21. R.L. Coble: *J. Appl. Phys.*, 1963, vol. 34, pp. 1679–82.

544 22. J. Weertman and J.R. Weertman: *Physical Metallurgy*, North-Holland Publishers,
545 Amsterdam, 1965, p. 793.

546 23. F.R. Larson and J. Miller: *Trans. ASME*, 1952, vol. 74, pp. 765–75.

547 24. W. Ren and R.W. Swindeman: *Journal of Pressure Vessel Technology*, 2014, vol. 136, p.
548 054001.

549 25. *ASME Boiler and Pressure Vessel Code*, American Society of Mechanical Engineers,
550 New York, NY, 2011.

551 26. API RP 530: *Recommended Practice for Calculation of Heater-Tube Thickness in*
552 *Petroleum Refineries*, American Petroleum Institute, Washington, D.C., 1978.

553 27. F.C. Monkman and N.J. Grant: *Proc. ASTM*, 1956, vol. 56, pp. 593–620.

554 28. R.W. Swindeman and D.L. Marriott: *ASME 1993 International Gas Turbine and*
555 *Aeroengine Congress and Exposition*, 1993, vol. 3A, pp. 1–11.

556 29. S. Ueda, T. Kameyama, T. Matsunaga, K. Kitazono, and E. Sato: *J. Phys. Conf. Ser.*,
557 2010, vol. 240, p. 012073.

30. T. Matsunaga, S. Ueda, and E. Sato: *Scripta Mater.*, 2010, vol. 63, pp. 516–19.

31. M. Kawasaki and T.G. Langdon: *J. Mater. Sci.*, 2012, vol. 47, pp. 7726–34.

32. N. Chawake, N.T.B.N. Koundinya, A.K. Srivastav, and R.S. Kottada: *Scripta Mater.*, 2015, vol. 107, pp. 63–66.

33. N. Bano, A.K. Koul, and M. Nganbe: *Metall. Mater. Trans. A*, 2014, vol. 45, pp. 1928–36.

34. J.H. Holland: *Adaptation in Natural and Artificial Systems*, Massachusetts Institute of Technology Press, Cambridge, MA, 1992.

35. R.L. Haupt and S.E. Haupt: *Practical Genetic Algorithms*, 2nd ed., John Wiley & Sons, Hoboken, NJ, 2004.

36. ASTM E8/E8M - 16a: *Standard Test Methods for Tension Testing of Metallic Materials*, American Society for Testing and Materials, West Conshohocken, PA, 2016.

37. ASTM E2627 - 10: *Standard Practice for Determining Average Grain Size Using Electron Backscatter Diffraction (EBSD) in Fully Recrystallized Polycrystalline Materials*, American Society for Testing and Materials, West Conshohocken, PA, 2010.

38. ASTM E112 - 12: *Standard Test Methods for Determining Average Grain Size*, American Society for Testing and Materials, West Conshohocken, PA, 2012.

39. ASTM E139 - 11: *Standard Test Methods for Conducting Creep, Creep-Rupture, and Stress-Rupture Tests of Metallic Materials*, American Society for Testing and Materials, West Conshohocken, PA, 2011.

40. F. Garofalo: *Trans. Metal. Soc. AIME*, 1963, vol. 227, pp. 351–56.

41. Data Sheets on the Elevated-Temperature Properties of Iron Based 21Cr-32Ni-Ti-Al Alloy for Heat Exchanger Seamless Tubes (NCF 800H TB), No. 26B, National Institute for Materials Science, Tsukuba, Ibaraki, Japan, 1998.

42. T. Back: *Evolutionary Algorithms in Theory and Practice: Evolution Strategies, Evolutionary Programming, Genetic Algorithms*, Oxford University Press, Oxford, UK, 1996.

584 43. L. Prechelt: *Neural Networks: Tricks of the Trade*, 2nd ed., Springer, Berlin, Heidelberg,
585 2012, pp. 53–67.

586 44. E. Whitley and J. Ball: *Critical Care*, 2001, vol. 6, p. 66.

587 45. F.R.N. Nabarro: *Mater. Sci. Eng. A*, 2004, vol. 387–389, pp. 659–64.

588 46. S. Huang, D.W. Brown, B. Clausen, Z. Teng, Y. Gao, and P.K. Liaw: *Metall. Mater.*
589 *Trans. A*, 2012, vol. 43, pp. 1497–508.

590 47. T. Shrestha, M. Basirat, I. Charit, G.P. Potirniche, and K.K. Rink: *Mater. Sci. Eng. A*,
591 2013, vol. 565, pp. 382–91.

592 48. R.W. Hayes, R.R. Unocic, and M. Nasrollahzadeh: *Metall. Mater. Trans. A*, 2015, vol. 46,
593 pp. 218–28.

594 49. L.J. Meng, J. Sun, and H. Xing: *J. Nucl. Mater.*, 2012, vol. 427, pp. 116–20.

595 50. M.T. Abdu, M.S. Soliman, E.A. El-Danaf, A.A. Almajid, and F.A. Mohamed: *Mater. Sci.*
596 *Eng. A*, 2012, vol. 531, pp. 35–44.

597 51. Data Sheets on the Elevated-Temperature Stress Relaxation Properties of Iron Based
598 21Cr-32Ni-Ti-Al Alloy for Corrosion-Resisting and Heat-Resisting Superalloy Bar (NCF
599 800H-B), No. 47, National Institute for Materials Science, Tsukuba, Ibaraki, Japan, 1999.

600 52. Data Sheets on the Elevated-Temperature Properties of Iron Based 21Cr-32Ni-Ti-Al
601 Superalloy for Corrosion-Resisting and Heat-Resisting Superalloy Plates (NCF 800H-P),
602 No. 27B, National Institute for Materials Science, Tsukuba, Ibaraki, Japan, 2000.